








Radial bound states in the continuum for polarization-invariant nanophotonics

Received: 4 February 2022

Accepted: 12 August 2022

Published online: 25 August 2022

 Check for updatesLucca Kühner ^{1,2}, Luca Sortino ^{1,2}, Rodrigo Berté ^{1,2,3}, Juan Wang^{1,2}, Haoran Ren ⁴, Stefan A. Maier ^{1,2,4,5}, Yuri Kivshar ⁶ & Andreas Tittl ^{1,2} ✉

All-dielectric nanophotonics underpinned by the physics of bound states in the continuum (BICs) have demonstrated breakthrough applications in nanoscale light manipulation, frequency conversion and optical sensing. Leading BIC implementations range from isolated nanoantennas with localized electromagnetic fields to symmetry-protected metasurfaces with controllable resonance quality (Q) factors. However, they either require structured light illumination with complex beam-shaping optics or large, fabrication-intense arrays of polarization-sensitive unit cells, hindering tailored nanophotonic applications and on-chip integration. Here, we introduce radial quasi-bound states in the continuum (radial BICs) as a new class of radially distributed electromagnetic modes controlled by structural asymmetry in a ring of dielectric rod pair resonators. The radial BIC platform provides polarization-invariant and tunable high-Q resonances with strongly enhanced near fields in an ultracompact footprint as low as $2 \mu\text{m}^2$. We demonstrate radial BIC realizations in the visible for sensitive biomolecular detection and enhanced second-harmonic generation from monolayers of transition metal dichalcogenides, opening new perspectives for compact, spectrally selective, and polarization-invariant metadevices for multi-functional light-matter coupling, multiplexed sensing, and high-density on-chip photonics.

The rise of optical metasurfaces has launched a variety of breakthrough applications ranging from negative refraction¹ and ultrathin optical elements² to photonic computation³. Similarly, bound states in the continuum⁴ (BICs) have been shown to underpin many fundamental oscillatory phenomena⁵ and can be employed for tailoring the lifetimes of resonant wave systems⁶. Initially discovered in quantum physics^{7,8} and also found in acoustics^{9,10} and ocean science¹¹, BICs have emerged as an intriguing concept in optics^{12–14}. In all-dielectric sub-wavelength structures, radiative losses of BIC-based systems can be precisely controlled by tailoring interferences of the constituent

resonant modes, producing sharp resonances with extremely high values of the quality (Q) factors. The BIC concept has therefore been employed for a variety of applications driven by such spectrally selective nanosystems, including multiplexed biospectroscopy^{15–18}, high-harmonic generation^{19,20}, and subwavelength lasing^{21–23}.

Two of the principal BIC implementations in nanophotonics are supercavity modes in isolated structures such as individual nanoantennas^{24,25} and resonances in symmetry-protected metasurfaces²⁶. Although single BIC structures offer a minimal footprint, careful electromagnetic engineering is required to

¹Chair in Hybrid Nanosystems, NanoInstitute Munich, Faculty of Physics, Ludwig-Maximilians-Universität München, Königinstrasse 10, 80539 Munich, Germany. ²Center for NanoScience (CeNS), Faculty of Physics, Ludwig-Maximilians-Universität München, Schellingstrasse 4, 80799 Munich, Germany. ³Instituto de Física, Universidade Federal de Goiás, 74001-970 Goiânia, GO, Brazil. ⁴School of Physics and Astronomy, Monash University, Clayton, VIC 3800, Australia. ⁵The Blackett Laboratory, Department of Physics, Imperial College London, London SW7 2AZ, UK. ⁶Nonlinear Physics Centre, Research School of Physics Australian National University, Canberra, ACT 2601, Australia. ✉ e-mail: andreas.tittl@physik.uni-muenchen.de

satisfy the demanding mode interference conditions of the hybridization of the Mie and Fabry–Pérot modes²⁴, restricting design flexibility and limiting the range of achievable Q factors. Based on these design constraints, such interference-type modes can only be excited with structured light illumination, further increasing experimental complexity. Moreover, the resonantly enhanced electric near fields are predominantly confined inside the structures, which is advantageous for material-intrinsic processes such as higher harmonic generation, but severely limits surface-driven light–matter interactions and sensing applications.

In contrast, metasurfaces based on all-dielectric resonators with broken in-plane inversion symmetry (Fig. 1a) offer both high-Q factors and strong near fields that extend considerably outside of the resonators, enabling cutting-edge applications in sensing^{16,18} and enhanced light–matter interaction^{20,27,28}. Significantly, symmetry-broken quasi-BICs (qBICs) provide straightforward tunability of the resonance position and Q factor via the geometrical scaling factor of the unit cell¹⁶ and the degree of asymmetry for increased design versatility. However, they require specific excitation polarizations, and the lateral on-chip footprints of metasurfaces supporting qBIC resonances in the visible spectrum usually exceed 100 μm^2 (see refs. 18,19), holding back their potential for device miniaturization, on-chip multiplexed sensors, and interactions with hybrid nanophotonic systems such as micron-sized individual layers of two-dimensional (2D) materials. Although their spatial extent can be reduced by transforming the system into a one-dimensional chain (Fig. 1b), this comes at a significant cost in terms of Q factor²⁹ (see Supplementary Note 1).

Here, we introduce the concept of radial quasi-bound states in the continuum (radial BICs) as a multi-application platform for sustaining polarization-invariant high-Q resonances with high surface sensitivity in a compact footprint. Notably, ring structures composed of as few as 12 unit cells can efficiently couple incident light into a pronounced radial quasi-BIC mode while providing flexible resonance tuning and strong surface-confined near fields. In our experimental realization, we achieve high-Q factors exceeding 500 in the red part of the visible spectrum and demonstrate the viability of our approach as a versatile BIC-based platform for biomolecular sensing and enhanced second-

harmonic generation in atomically thin 2D semiconductor molybdenum diselenide (MoSe_2) monolayers, all in a spatial footprint as small as 2 μm^2 .

Results

Design and implementation of the radial BIC concept

The symmetry-protected and radially distributed electromagnetic BIC states are accessed through a carefully designed ring structure incorporating symmetry-broken double rod unit cells, where individual resonators are rotated to satisfy radial alignment (Fig. 1c). At resonance, adjacent rods support opposing electric dipoles, which leads to a suppression of the total dipole moment and consequently of the radiative losses in the system. In contrast to previous 2D or 1D resonator arrangements, our approach leverages a semi-infinite ring geometry^{30,31}, providing a polarization-invariant optical response and avoiding edge effects, which allows a higher number of resonator elements to participate in the qBIC state for increased resonance quality³². Owing to the unique circular arrangement, the coupling between elements over the entire ring is improved as well, resulting in much higher Q factors compared to linear resonator chains (Supplementary Fig. S4). As a result, the radial BIC platform provides the highest quality factor to footprint ratio amongst comparable BIC-based nanophotonic approaches^{18–20,32} (Fig. 1). Furthermore, even though neighboring resonators are set at a small angle with respect to each other, the radial arrangement of rods with identical lengths produces a non-radiating BIC state with negligible coupling to the far field (Fig. 2a).

One of the key parameters to control the optical characteristics of the radial BIC mode is the asymmetry parameter ΔL , i.e., the length difference between the two constituent rods of the unit cell. In the symmetric case ($\Delta L = 0$), we observe a BIC-like state, which is decoupled from the radiation continuum and exhibits negligible electromagnetic near-field enhancement (Fig. 2a). For nonzero asymmetry ($\Delta L > 0$), the BIC transforms into a radial quasi-BIC mode (termed radial BIC from now on), which can be accessed from the far field, demonstrating strong field enhancements and the characteristic field pattern of oppositely oriented electric dipole moments observed in asymmetric metasurfaces²⁶ (Fig. 2b). Due to the engineered inter-resonator coupling within the ring, linearly polarized light efficiently couples to the full radial BIC mode extended along the ring and excites spectrally distinct resonances with high-Q factors (Supplementary Fig. S1). Our numerical calculations confirm the presence of highly enhanced near fields outside the resonator volume and highlight how the field magnitude can be tailored via the structural asymmetry (Fig. 2b). We engineer the radial BIC system to exhibit high-Q resonances at around 770 nm and find that the corresponding numerically simulated Q factors exceed 8000 toward the smallest asymmetries (Supplementary Fig. S2). Furthermore, we observe a clear correlation between the electric near fields (Fig. 2b, for field intensities, see Supplementary Fig. S6) and the values of the Q factors, where the lowest asymmetry is associated with the maximum values of both parameters.

Symmetry-broken ring structures with varying geometry were fabricated from a 120 nm thick amorphous silicon layer on a glass substrate using electron beam lithography and reactive ion etching (see “Methods” for details). All measurements shown in the manuscript are based on ring structures with 24 annular unit cells and a base rod length $L_0 = 335$ nm with width $w = 115$ nm. Symmetry-breaking is introduced by shortening one rod within the unit cell as indicated by the corresponding asymmetry parameter ΔL (Fig. 2b). The choice of the asymmetries is based on tradeoff between highest Q factors (and associated strong near fields) and the resulting modulation of the radial BIC resonances in the optical experiments. Although higher field enhancements and ultrahigh Q factors above 8000 are numerically predicted for asymmetries approaching $\Delta L = 0$ nm (see Supplementary

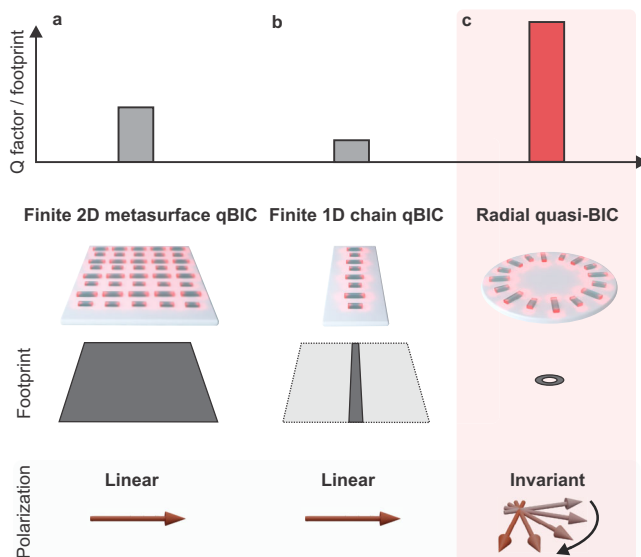


Fig. 1 | Conceptual advantages of radial quasi-bound states in the continuum (radial BICs). Established symmetry-broken quasi-BIC geometries, such as 2D metasurfaces (a), and 1D chains (b), exhibit large footprints, moderately high Q factors, and require polarization-dependent excitation. The radial BIC concept (c) combines a tiny footprint with high-Q factors in the visible. Above all, the radial BIC platform provides the highest Q factor per footprint ratio compared to other 1D and 2D BIC-based platforms, as shown here.

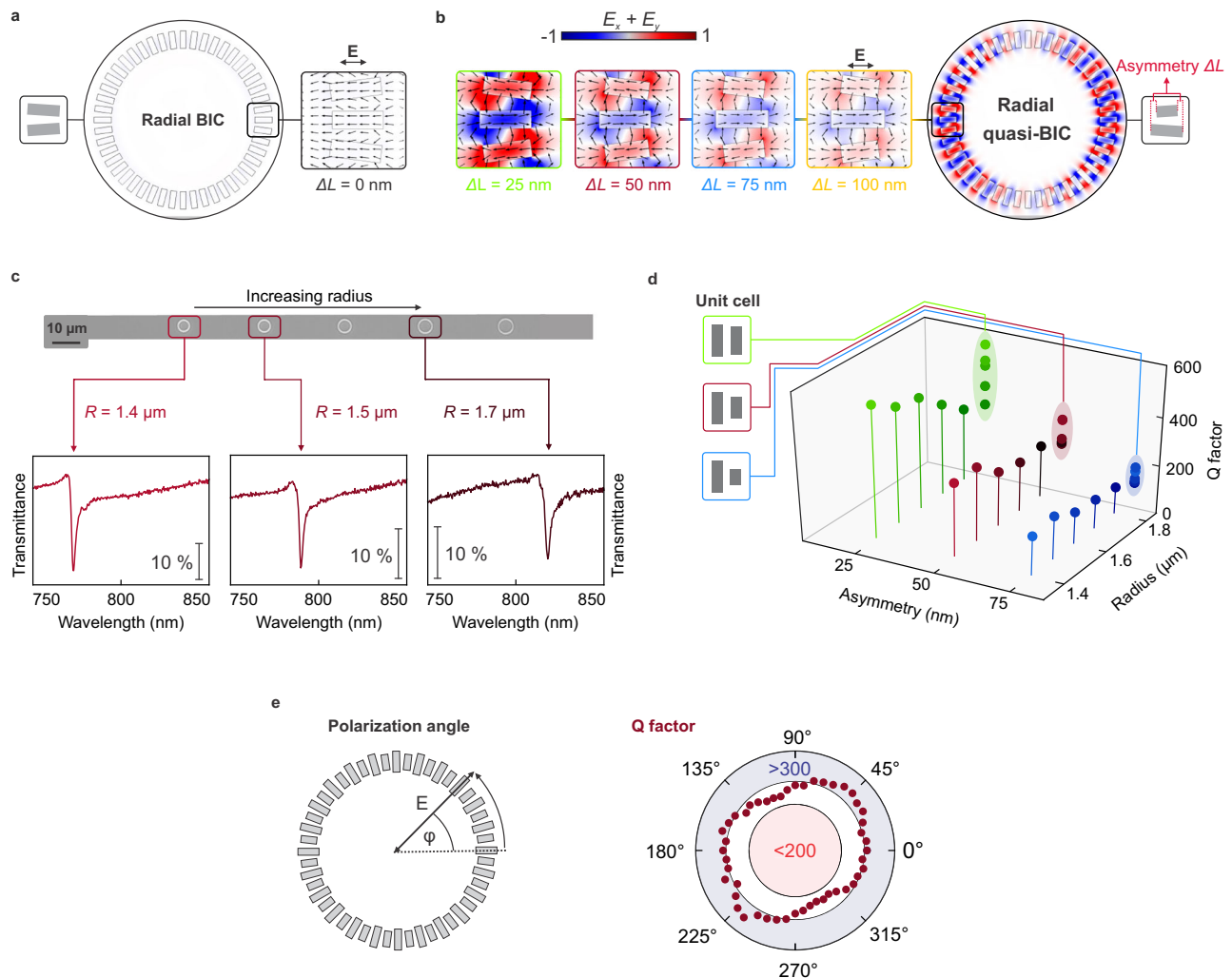


Fig. 2 | Versatile radial BIC resonances and polarization invariance. Electric near fields for a symmetric radial BIC ($\Delta L = 0$ nm) in **a** and several symmetry-broken radial quasi-BIC ($\Delta L > 0$ nm) geometries in **b**. **c** Optical transmittance spectra of the radial BIC structures show a resonance redshift with increasing radii, as illustrated in the gray-scale optical micrograph. **d** Dependence of the

quality factor on the ring radius R and the unit cell asymmetry ΔL . Quality factors exceed 500 for $\Delta L = 25$ nm in the visible wavelength range. **e** The radial BIC geometry shows polarization invariance as observed by the weak dependence of the resonance quality factor on the polarization angle of the incident light φ .

Fig. S2), an optimum parameter range was found for asymmetry values around $\Delta L = 25$ nm, taking into account nanofabrication accuracy and the noise characteristics of our spectroscopy setup.

Optical characterization of the structures is carried out with a commercial confocal microscopy setup under collimated white light illumination. We first examine the optical response of the radial BIC structures with different radii and find precise tuning of the resonance wavelength via the ring radius R (Fig. 2c). Importantly, our versatile design provides additional degrees of freedom for tailoring the resonance, such as the number of unit cells constituting the ring and the base length L_0 of the all-dielectric rods (Supplementary Fig. S8).

Consistent with numerical simulations, we observe the highest resonance sharpness for the smallest values of the asymmetry ΔL with Q factors exceeding 500 (Fig. 2d, for fitting details and full spectra, see Supplementary Figs. S9 and S10). To our knowledge, this is one of the highest Q factors measured for symmetry-broken qBIC resonances in the visible wavelength range. For all asymmetries, the Q factor increases with decreasing radii (Supplementary Fig. S3), which we attribute to the improved coupling between the resonators. This scaling behavior is consistent with the fact that the coupling vanishes for infinite radii with infinite spacing between the resonators.

Strikingly, the annular arrangement of the resonator elements renders the Q factor mostly invariant under rotations of the incident polarization direction of light³³, maintaining a value above 200 throughout the angular range (Fig. 2e). We attribute the observed spectral polarization invariance to the inherent C_{24} symmetry of our ring design which congruently transforms the ring onto itself for a rotation by one unit cell (15°). Furthermore, we do not observe any polarization angle dependence of the spectral response for smaller rotation angles ($0 \leq \varphi \leq 15^\circ$, see Supplementary Fig. S7). As a result, we conclude that the spectral response of the radial BIC is fully polarization-invariant for any arbitrary polarization angle. Crucially, this polarization-independent performance enables simplified experimental measurements and greatly eases practical device applications.

Enhanced biomolecular sensitivity

We leverage the high-Q resonances and strong surface-confined near fields of the radial BIC platform to demonstrate biomolecular sensing for different ring geometries and asymmetries based on a biotin-streptavidin binding bioassay (Fig. 3a). As an initial step, we assess the refractometric sensing performance by varying the local refractive index around the ring structure (see “Methods” for details) by means of magnetron sputtering of conformal silicon dioxide (SiO_2) thin films with

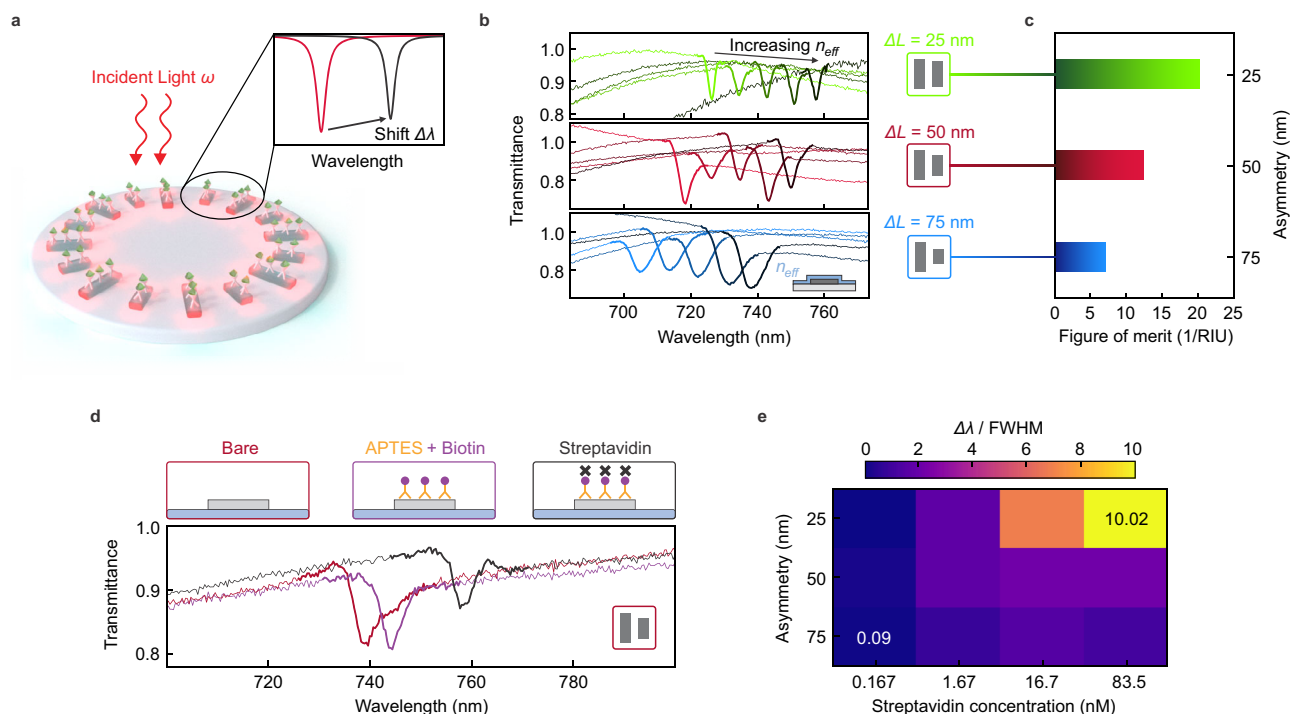


Fig. 3 | Refractive index and molecular biosensing with radial BICs. **a** Sketch of the biosensing experiments. The ring structures are functionalized with capture antibodies, and shifts in the spectral position of the resonance are recorded for the binding of different concentrations of biomolecules.

b Optical transmittance spectra of three-unit cell asymmetries ΔL with $R = 1.5 \mu\text{m}$ covered with different thicknesses of conformal SiO_2 thin films.

c Corresponding figure of merit for bulk refractive index sensing.

d Transmittance spectra for a ring with $\Delta L = 50 \text{ nm}$ and $R = 1.6 \mu\text{m}$ after each functionalization and molecular binding step as indicated in the color-coded boxes. **e** Map of biomolecular sensing performance. Measured resonance shifts normalized to the respective FWHM for three different asymmetries dependent on streptavidin concentrations.

increasing thickness. Pronounced resonance shifts for all asymmetries can be detected, depending on the SiO_2 layer thicknesses (Fig. 3b). For the calculation of the bulk refractive index sensitivity S_B (BRIS), the resonance shifts mediated by the thin films are converted by considering both the electric near-field decay length of the resonators and the film thickness as introduced previously³⁴ (see “Methods”).

Based on these BRIS values, we find that the sensing figure of merit

$$\text{FOM} = S_B / \text{FWHM}, \quad (1)$$

where FWHM is the resonance full width at half maximum, is clearly correlated with the asymmetry of the radial BIC structures, with the highest FOM of above 20 per refractive index (RIU) observed for the lowest asymmetry (Fig. 3c). Despite the much smaller footprint, the FOM values of our radial BIC geometry for biomolecular sensing are mostly comparable with large array-based approaches relying on symmetry-protected metasurfaces¹⁸. Nevertheless, we believe that the FOM can be substantially boosted by utilizing even smaller asymmetries or by further engineering the inter-rod coupling, e.g., by optimizing the resonator shape. Additional advantages of the radial BIC approach can be realized by a concentric arrangement of several rings for multiplexed operation without increasing the footprint, or by integrating multiple rings with identical resonance wavelengths to enhance light absorption efficiency per area.

For the implementation of a model multistep bioassay, we first functionalize our structures with (3-Aminopropyl) triethoxysilane (APTES), followed by the attachment of biotin molecules and the binding of different concentrations of streptavidin protein. After each step, we observe a clear redshift of the radial BIC resonance (Fig. 3d), induced by the higher number of molecules on the surface and the associated increase of the environmental refractive index. To compare

the biomolecular sensing performance for all asymmetries, we normalize the resonance shift by the respective FWHM and plot it for each streptavidin concentration to obtain a map of biomolecular sensing performance (Fig. 3e).

Notably, a clear and streptavidin-dependent sensor response over a broad range of concentrations and resonance linewidths is observed. Depending on the sensitivity and spectral resolution of the spectroscopic equipment in experiments and thus the required resonance modulations as well as Q factors, we demonstrate a wide parameter space for picking the appropriate structural asymmetry. Especially, field-deployed applications with low spectral resolution may require lower Q resonances—whereas when pushing for highest sensitivity, high-Q resonances and consequently a high FOM is favored. Our versatile radial BIC platform allows to cover all such use cases in an ultrasmall footprint, pushing the limits of on-chip multiplexing applications for biosensing and opening up new avenues for the precise on-demand tailoring of FOM, Q factor, resonance position, and resonance modulation.

Enhanced SHG in an evanescently coupled monolayer of MoSe_2

To further demonstrate the versatility of our design, we employed the radial BIC platform for enhanced light–matter interaction between the all-dielectric resonator system and a two-dimensional excitonic material^{20,35,36}. Specifically, we demonstrate and localize enhanced second-harmonic generation (SHG) in a non-centrosymmetric monolayer crystal of the transition metal dichalcogenide (TMD) MoSe_2 , facilitated by the highly enhanced electromagnetic near fields that are associated with the radial BIC resonances. For this purpose, we deterministically transferred a monolayer of MoSe_2 on top of the radial BIC platform (Fig. 4a). Crucially, this experiment is enabled by the low footprint of the radial BIC platform, which allows full spatial overlap between the micron-sized MoSe_2 layer and the ultracompact ring geometry. Atomic force microscopy (AFM) imaging confirms the

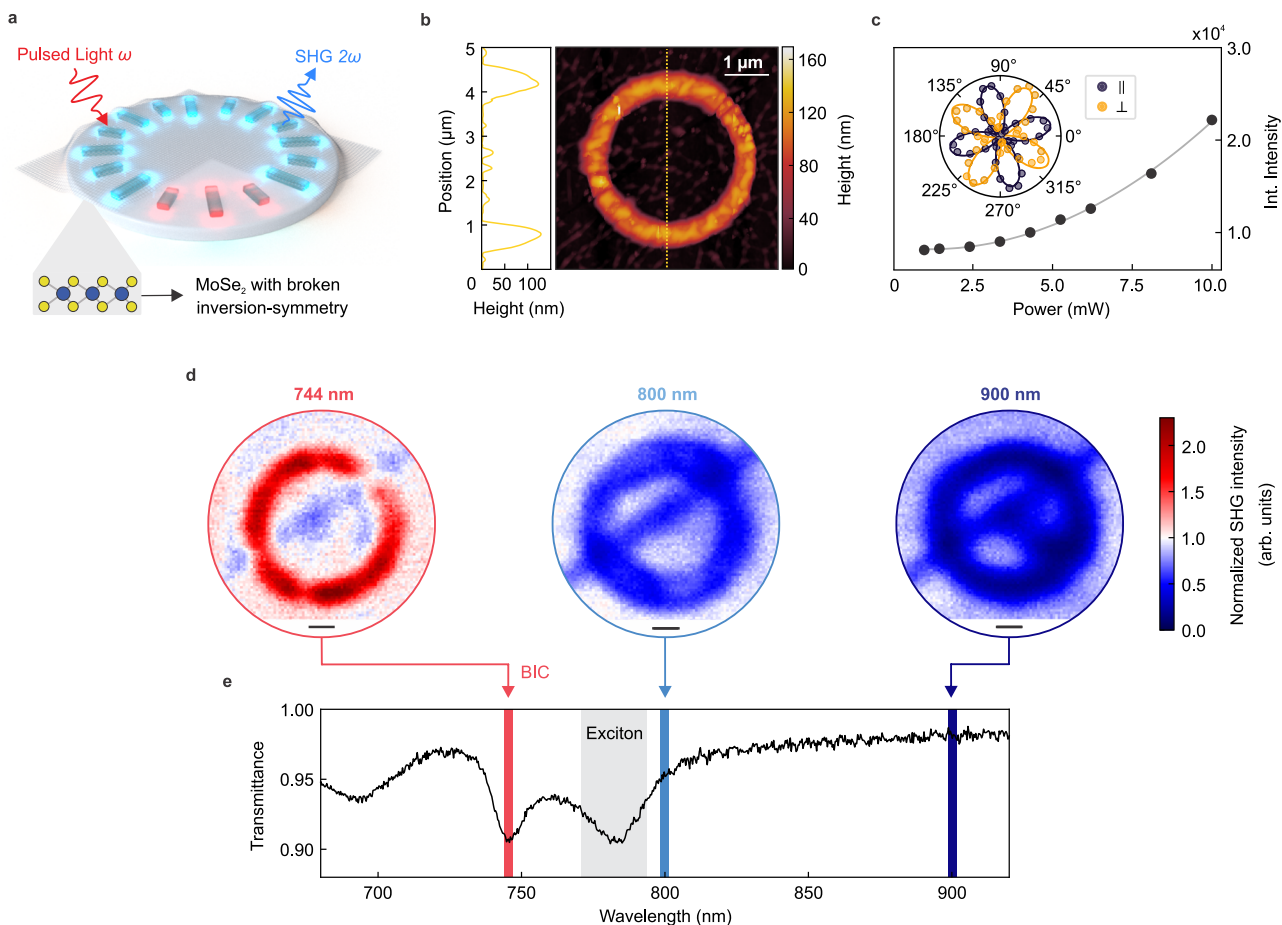


Fig. 4 | Radial BIC-enhanced second-harmonic generation in a MoSe₂ monolayer. **a** Schematic depiction of a MoSe₂ monolayer covering the ring structures while being illuminated by a pulsed excitation laser. **b** AFM image showing the coverage of the flake on top of the ring. **c** Integrated second-harmonic generation (SHG) signal for an excitation wavelength of $\lambda = 744$ nm from the MoSe₂ monolayer on a bare substrate showing a quadratic dependence (grey fit line). Inset: Polarization-resolved SHG signal from the MoSe₂ monolayer in either parallel or

perpendicular detection (see “Methods”). **d** SHG maps for the ring displayed in **b** taken at different excitation wavelengths. SHG enhancement is only present for an excitation wavelength resonant with the radial BIC. In contrast, for the off-BIC excitation, we observe the expected suppression of the SHG signal due to strain. Scale bar: 300 nm. **e** Transmittance spectrum of the ring structure ($\Delta L = 50$ nm) covered with MoSe₂ monolayer clearly showing the spectral signatures of the radial BIC resonance (744 nm) next to the absorption line of the exciton (785 nm).

homogeneous coverage of the resonators (Fig. 4b) and indicates that the monolayer is in good contact with the silicon structures. In Fig. 4c, we show the quadratic dependence of the integrated SHG signal on the input power for the monolayer together with its polarization-resolved signal (inset, see “Methods”), confirming the origin of the signal from the nonlinear harmonic light generation in the atomically thin crystal³⁷.

To demonstrate spectrally selective SHG, we excite the coupled system of a MoSe₂ monolayer on top of a tailored radial BIC structure at three different excitation wavelengths with the use of a tunable femtosecond pulsed laser (Fig. 4d, e, see “Methods” for details). For this purpose, we choose a ring with $\Delta L = 50$ nm to balance the high near-field enhancements with a sufficient resonance modulation. Although we expect even higher near-field and thus SHG enhancements for smaller asymmetries (see Supplementary Fig. S6), these resonances are often strongly damped by the TMD monolayer in experiments. For our SHG measurements, we excite the system at 744 nm in resonance with the radial BIC mode, at 800 nm close to the MoSe₂ exciton peak, and at 900 nm, spectrally distinct from both the exciton and the radial BIC resonance (Fig. 4e). At each excitation wavelength, we raster the focused laser beam across the sample, direct the light to an avalanche single photon detector, and plot the obtained SHG signal intensity for each point. In Fig. 4d, we show the maps of the SHG signal on the ring normalized to the bare MoSe₂ monolayer flake to guarantee consistency between the measurements and to eliminate

wavelength-dependent processes such as detector and SHG efficiency as well as transmission of the signal in the optical beam path (see Supplementary Fig. S11b for raw data without background).

For radial BIC-resonant excitation, we observe a fivefold SHG intensity enhancement confined to the ring structure, illustrating the highly localized generation of the second-harmonic signal. In contrast, for off-resonant excitation, we observe a suppression of the SHG (Fig. 4d) within the same region. The suppression of the SHG signal when excited spectrally apart from the radial BIC resonance can be attributed to strain introduced in the monolayer TMD by the ring structure³⁸, which is outperformed by the highly enhanced near fields of the resonant excitation. The wavelength dependence is a clear indication that the SHG enhancement is driven by the locally enhanced electromagnetic near fields of the radial BIC resonances. We further examined the SHG signal originating from the bare silicon radial BIC structures and observed only a negligible contribution to the overall SHG intensity (see Supplementary Fig. S11a).

We further conducted control experiments where we suppressed the radial BIC resonance by investigating a symmetric structure ($\Delta L = 0$ nm, Supplementary Fig. S12). In this case, we observe no enhancement of the SHG signal when the monolayer is on top of symmetric rings and probed at the wavelength associated with the radial BIC resonance at 744 nm, further confirming that the observed SHG enhancement arises from the near-field coupling of the MoSe₂ monolayer with the

radial BIC mode. We also perform linearly polarized excitation and show the corresponding polarization-dependent SHG maps in Supplementary Fig. S13. Crucially, the SHG generation experiments are highly facilitated by the compact footprint and polarization invariance of our ring geometry since the constraints on the spatial alignment and orientation of the TMD monolayer are released.

Discussion

We have introduced a new platform for enhancing light-matter interactions that combines all benefits of symmetry-broken qBIC approaches while providing at least 50 times less footprint compared to extended 2D metasurfaces¹⁹. We have demonstrated the enormous potential of our nanophotonic framework by showing highly sensitive biomolecular detection experiments as well as localized SHG enhancement in a monolayer of MoSe₂. Our results enable on-demand tailoring of high-Q resonances in ultracompact optical devices for a variety of applications such as integrated multiresonant and hybrid sensors as well as photonic modes for coupled polariton physics.

Methods

Simulations

Numerical calculations were performed in the frequency domain by obtaining full-wave solutions of Maxwell's equations using the commercially available RF module of the finite element solver COMSOL Multiphysics. Port boundary conditions were employed for the excitation of the structures and perfectly matched layers (PML) domains for the absorption of propagating waves. A dispersionless refractive index of $n = 1.45$ was employed for the SiO₂ substrate, while the dispersive refractive index of the amorphous silicon film, as measured via ellipsometry, was used for the resonators. The field normalization was performed considering the solution obtained for the sum of the in-plane components of the electric field ($E_x + E_y$) using as a reference the smallest chosen asymmetry ($\Delta L = 25$ nm) to highlight the reduction in field enhancement for larger asymmetries (for near-field intensities, see Supplementary Fig. S6).

Radial BIC fabrication

Prior to fabrication, the fused silica substrates were cleaned in an ultrasonic bath at 55 °C with acetone and rinsed with isopropanol (IPA) followed by an oxygen plasma etching step to guarantee the cleanliness of the substrates. Afterwards, a 120 nm thick amorphous silicon (a-Si) layer was deposited at 250 °C via plasma-enhanced chemical vapor deposition on top of the silica substrate. We used a 180 nm thick double layer of the positive tone resist poly (methyl methacrylate) (PMMA) with different chain lengths (495 k and 950 k) to guarantee an undercut of the resist after development which aids for the liftoff process. We baked each resist layer at 170 °C for 3 min. A conductive polymer (E-Spacer 300Z) was deposited on top of the PMMA double layer to suppress charge accumulations on the substrate.

Electron beam lithography (EBL) was utilized to define the nanostructure pattern into the resist using 30 kV acceleration voltage for maximum edge sharpness of our nanostructures. The illuminated resist was developed in a 3:1 IPA:MIBK (Methyl isobutyl ketone) for 90 seconds after the organic polymer has been washed off by a water bath for 10 seconds. We used a combination of 20 nm silicon dioxide (SiO₂) and 25-nm chromium (Cr) layer deposited via electron beam evaporation as hard mask where the SiO₂ layer served as an effective diffusion barrier for the Cr atoms which can introduce severe losses within the silicon radial BIC structures. The liftoff of the metal structures was performed in special remover (Microsposit remover 1165) at 80 °C overnight. The hard mask pattern was transferred into the silicon film via inductively coupled reactive ion etching (ICP-RIE) by chlorine and fluorine chemistry. After removing the Cr hard mask with a chromium wet etch, we removed the SiO₂ hard mask by a final ICP-RIE step to obtain the pure silicon nanostructures.

Optical measurements

The optical characterization of our radial BIC structures was conducted with a commercial white light transmission microscopy setup (WiTec alpha300 series). Importantly, the samples were illuminated with collimated white light from the backside and the transmitted signal was collected with a $\times 50$ objective (NA = 0.8). Because of the collimated and linearly polarized illumination, good agreement could be obtained with the simulations, where the same illumination conditions were assumed. The collected light was focused into a fiber which is coupled to a grating-spectrometer equipped with a silicon CCD camera that we used to acquire white light transmittance spectra. All the transmittance spectra shown were referenced to the bare SiO₂ substrate. We note that the interaction cross-section of the white light depends on the ring radius of the constituent geometry, thus, different radii lead to different transmitted white light intensities potentially causing slightly different resonance modulations. This behavior, however, did not impede our physical observations and our conclusions are in excellent agreement with the theory.

Biofunctionalization

The radial BIC structures were treated by piranha solution and oxygen plasma cleaning processes to activate the structure surface with a high amount of hydroxyl radicals (-OH). Then, a silanization protocol using (3-aminopropyl)triethoxysilane (APTES, 10% v/v in ethanol, overnight) was used to modify the structure surface with NH₂ groups, which is ready to capture sulfo-NHS-biotin molecules (ThermoFisher Scientific, Mn = 443.4, as a linker between the radial resonators and target molecules). The sulfo-NHS-biotin molecules dissolved in phosphate buffered saline (1 \times , PBS) buffer solution were drop-casted on the structures with a volume of 40 μ L and allowed to incubate for 2 h at room temperature, followed by a rinsing step using 1 \times PBS buffer and drying under N₂ flow. Afterwards, the biotin-immobilized resonators were incubated in target analyte solutions of streptavidin with varying concentrations for 2 h at room temperature. Once the streptavidin incubation finished, the resonators were rinsed with PBS buffer, dried using N₂ flow, and transferred to the optical characterization setup.

Determination of quality factors

For the Q factor extraction of our sharp radial BIC resonances, we employed temporal coupled mode theory³⁹ to extract the linewidth γ of the resonance (see Supplementary Fig. S9) using

$$T = |ie^{i\phi}t_0 + \frac{\gamma_r}{\gamma_r + \gamma_i + i(\lambda - \lambda_{\text{res}})}|^2 \quad (2)$$

where $e^{i\phi}t_0$ accounts for the background transmission and controls the shape of the resonance. The Q factor was calculated as³²

$$Q = \frac{\lambda_{\text{res}}}{2\gamma}, \quad (3)$$

$$\gamma = \gamma_i + \gamma_r, \quad (4)$$

where λ_{res} is the resonance wavelength and γ_i and γ_r is the intrinsic and radiative loss rate, respectively. The same fitting approach was applied for the simulated and experimental transmittance spectra to ensure consistent Q factors.

Extraction of bulk refractive index sensitivity

The bulk refractive index sensitivity was extracted from the surface sensitivity S_s , which can be calculated using

$$S_s = \frac{\Delta\lambda_{\text{res}}}{\Delta n_s}, \quad (5)$$

where n_s is the refractive index of the conformally deposited SiO₂ thin film³⁴. Similar to the bulk figure of merit for refractive index sensing, we defined the figure of merit for surface sensitivity as

$$\text{FOM}_S = \frac{S_S}{\text{FWHM}}, \quad (6)$$

with FWHM being the full width at half maximum of the radial BIC resonance. From the figure of merit for surface sensitivity, we could calculate the figure of merit for bulk refractive index sensitivity via

$$\text{FOM}_B = \frac{\text{FOM}_S}{1 - \exp(-2h/l_d)}, \quad (7)$$

where h is the thickness of the thin films and l_d is the decay length of the electric near fields that we extracted from simulations as 44.7 nm.

2D material fabrication and transfer

The exfoliation of a large area atomically thin monolayers of molybdenum diselenide (MoSe₂) was done via mechanical exfoliation from a seed crystal (HQ Graphene) with blue tape (Nitto) onto polydimethylsiloxane (PDMS) stamps. Suited monolayers for transfer were identified with an optical microscope, and monolayers were confirmed by photoluminescence imaging on the PDMS substrate. For the transfer, we used a home-built transfer setup with motorized z stage to control the stamp movement.

SHG measurements

We employed the output of a tunable Ti:sapphire laser (Coherent Chameleon Ultra II) to selectively excite the SHG signal from the MoSe₂ monolayer sample mounted in an inverted microscope setup and collected in back reflection geometry. The sample was placed on a motorized stage allowing the mapping of the sample surface. The SHG signal was isolated from the excitation beam with a short pass filter (Semrock) and collected with an avalanche photodiode detector (Micro Photon Devices). The polarization-resolved SHG signal was obtained by rotating the linear polarization of the excitation beam with a halfwave plate. The signal was then filtered with a linear polarizer, either parallel or perpendicular to the initial excitation laser polarization, before being collected in a grating-spectrometer equipped with a silicon CCD camera (Princeton Instruments).

Data availability

The main data supporting the findings of this study are available within the article and its Supplementary Information files. Extra data are available from the corresponding author upon reasonable request.

References

- Valentine, J. et al. Three-dimensional optical metamaterial with a negative refractive index. *Nature* **455**, 376–379 (2008).
- Lin, D., Fan, P., Hasman, E. & Brongersma, M. L. Dielectric gradient metasurface optical elements. *Science* **345**, 298–302 (2014).
- Silva, A. et al. Performing mathematical operations with metamaterials. *Science* **343**, 160–163 (2014).
- Hsu, C. W., Zhen, B., Stone, A. D., Joannopoulos, J. D. & Soljačić, M. Bound states in the continuum. *Nat. Rev. Mater.* **1**, 16048 (2016).
- Azzam, S. I. & Kildishev, A. V. Photonic bound states in the continuum: from basics to applications. *Adv. Optical Mater.* **9**, 2001469 (2021).
- Koshelev, K., Favraud, G., Bogdanov, A., Kivshar, Y. & Fratallocchi, A. Nonradiating photonics with resonant dielectric nanostructures. *Nanophotonics* **8**, 725–745 (2019).
- von Neuman, J. & Wigner, E. P. Über merkwürdige diskrete Eigenwerte. *Phys. Z.* **30**, 465–467 (1929).
- Stillinger, F. H. & Herrick, D. R. Bound states in the continuum. *Phys. Rev. A* **11**, 446–454 (1975).
- Parker, R. Resonance effects in wake shedding from parallel plates: some experimental observations. *J. Sound Vib.* **4**, 62–72 (1966).
- Cumpsty, N. A. & Whitehead, D. S. The excitation of acoustic resonances by vortex shedding. *J. Sound Vib.* **18**, 353–369 (1971).
- Linton, C. M. & McIver, P. Embedded trapped modes in water waves and acoustics. *Wave Motion* **45**, 16–29 (2007).
- Plotnik, Y. et al. Experimental observation of optical bound states in the continuum. *Phys. Rev. Lett.* **107**, 183901 (2011).
- Marinica, D. C., Borisov, A. G. & Shabanov, S. V. Bound states in the continuum in photonics. *Phys. Rev. Lett.* **100**, 183902 (2008).
- Hsu, C. W. et al. Observation of trapped light within the radiation continuum. *Nature* **499**, 188–191 (2013).
- Leitis, A. et al. Angle-multiplexed all-dielectric metasurfaces for broadband molecular fingerprint retrieval. *Sci. Adv.* **5**, eaaw2871 (2019).
- Tittl, A. et al. Imaging-based molecular barcoding with pixelated dielectric metasurfaces. *Science* **360**, 1105–1109 (2018).
- Jahani, Y. et al. Imaging-based spectrometer-less optofluidic biosensors based on dielectric metasurfaces for detecting extracellular vesicles. *Nat. Commun.* **12**, 3246 (2021).
- Yesilkoy, F. et al. Ultrasensitive hyperspectral imaging and biodection enabled by dielectric metasurfaces. *Nat. Photonics* **13**, 390–396 (2019).
- Liu, Z. et al. Giant enhancement of continuous wave second harmonic generation from few-layer GaSe coupled to high-Q quasi bound states in the continuum. *Nano Lett.* **20**, 5309–5314 (2021).
- Bernhardt, N. et al. Quasi-BIC resonant enhancement of second-harmonic generation in WS₂ monolayers. *Nano Lett.* **20**, 5309–5314 (2020).
- Kodigala, A. et al. Lasing action from photonic bound states in continuum. *Nature* **541**, 196–199 (2017).
- Hwang, M. et al. Ultralow-threshold laser using super-bound states in the continuum. *Nat. Commun.* **12**, 4135 (2021).
- Huang, C. et al. Ultrafast control of vortex microlasers. *Science* **367**, 1018–1021 (2020).
- Rybin, M. V. et al. High-Q supercavity modes in subwavelength dielectric resonators. *Phys. Rev. Lett.* **119**, 243901 (2017).
- Koshelev, K. et al. Subwavelength dielectric resonators for nonlinear nanophotonics. *Science* **367**, 288–292 (2020).
- Koshelev, K., Lepeshov, S., Liu, M., Bogdanov, A. & Kivshar, Y. Asymmetric metasurfaces with high-Q resonances governed by bound states in the continuum. *Phys. Rev. Lett.* **121**, 193903 (2018).
- Koshelev, K. et al. Nonlinear metasurfaces governed by bound states in the continuum. *ACS Photonics* **6**, 1639–1644 (2019).
- Kravtsov, V. et al. Nonlinear polaritons in a monolayer semiconductor coupled to optical bound states in the continuum. *Light Sci. Appl.* **9**, 1–8 (2020).
- Sadrieva, Z. F. et al. Experimental observation of a symmetry-protected bound state in the continuum in a chain of dielectric disks. *Phys. Rev. A* **99**, 053804 (2019).
- Bulgakov, E. N. & Sadreev, A. F. Nearly bound states in the radiation continuum in a circular array of dielectric rods. *Phys. Rev. A* **97**, 033834 (2018).
- Han, H.-L., Li, H., Lü, H. & Liu, X. Trapped modes with extremely high quality factor in a circular array of dielectric nanorods. *Opt. Lett.* **43**, 5403 (2018).
- Liu, Z. et al. High-Q quasibound states in the continuum for nonlinear metasurfaces. *Phys. Rev. Lett.* **123**, 253901 (2019).
- Sayanskiy, A., Danaeifar, M., Kapitanova, P. & Miroshnichenko, A. E. All-dielectric metalattice with enhanced toroidal dipole response. *Adv. Optical Mater.* **6**, 1800302 (2018).

34. Špačková, B., Wrobel, P., Bocková, M. & Homola, J. Optical biosensors based on plasmonic nanostructures: a review. *Proc. IEEE* **104**, 2380–2408 (2016).
35. Sortino, L. et al. Enhanced light-matter interaction in an atomically thin semiconductor coupled with dielectric nano-antennas. *Nat. Commun.* **10**, 5119 (2019).
36. Xiao, S., Qin, M., Duan, J. & Liu, T. Robust enhancement of high-harmonic generation from all-dielectric metasurfaces enabled by polarization-insensitive bound states in the continuum. *Opt. Lett.* **46**, 633 (2022).
37. Psilodimitrakopoulos, S. et al. Twist angle mapping in layered WS₂ by polarization-resolved second harmonic generation. *Sci. Rep.* **9**, 14285 (2019).
38. Wang, K. et al. Strain tolerance of two-dimensional crystal growth on curved surfaces. *Sci. Adv.* **5**, eaav4028 (2019).
39. Fan, S., Suh, W. & Joannopoulos, J. D. Temporal coupled-mode theory for the Fano resonance in optical resonators. *J. Optical Soc. Am. A* **20**, 569 (2003).

Acknowledgements

The authors thank Philipp Altpeter for fabrication advices, Thomas Weber for the implementation of the fitting routines, as well as Christoph Hohmann for support with rendered images. Our studies were funded by the Deutsche Forschungsgemeinschaft (DFG, German Research Foundation) under grant numbers EXC 2089/1—390776260 (Germany's Excellence Strategy) and TI 1063/1 (Emmy Noether Program), the Bavarian program Solar Energies Go Hybrid (SolTech), the Center for NanoScience (CeNS), the Australian Research Council (the grant DP210101292), the International Technology Center Indo-Pacific (ITC IPAC) and Army Research Office (contract No. FA520921P0034), and the National Council for Scientific and Technological Development (CNPq) (PDJ 2019—150393/2020-2). S.A.M. additionally acknowledges the EPSRC (EP/W017075/1) and the Lee-Lucas Chair in Physics. L.S. acknowledges funding support through a Humboldt Research Fellowship from the Alexander von Humboldt Foundation. H.R. acknowledges funding support from the DECRA Project (DE220101085) from the Australian Research Council.

Author contributions

L.K. and A.T. conceived the idea and planned the research. L.K. fabricated the radial BIC samples. L.K., L.S., J.W., and H.R. performed optical measurements. L.K. and A.T. analyzed the data. R.B. did numerical simulations. R.B. and Y.K. performed the theoretical analysis of the radial

BIC platform. S.M., Y.K., and A.T. supervised the project. All authors discussed the results and contributed to the writing of the manuscript.

Funding

Open Access funding enabled and organized by Projekt DEAL.

Competing interests

The authors declare no competing interests.

Additional information

Supplementary information The online version contains

supplementary material available at <https://doi.org/10.1038/s41467-022-32697-z>.

Correspondence and requests for materials should be addressed to Andreas Tittl.

Peer review information *Nature Communications* thanks Hong-Gyu Park and the other anonymous reviewer(s) for their contribution to the peer review of this work.

Reprints and permission information is available at <http://www.nature.com/reprints>

Publisher's note Springer Nature remains neutral with regard to jurisdictional claims in published maps and institutional affiliations.

Open Access This article is licensed under a Creative Commons Attribution 4.0 International License, which permits use, sharing, adaptation, distribution and reproduction in any medium or format, as long as you give appropriate credit to the original author(s) and the source, provide a link to the Creative Commons license, and indicate if changes were made. The images or other third party material in this article are included in the article's Creative Commons license, unless indicated otherwise in a credit line to the material. If material is not included in the article's Creative Commons license and your intended use is not permitted by statutory regulation or exceeds the permitted use, you will need to obtain permission directly from the copyright holder. To view a copy of this license, visit <http://creativecommons.org/licenses/by/4.0/>.

© The Author(s) 2022